A Novel Vortex Synthetic Aperture Radar Imaging System: Decreasing the Pulse Repetition Frequency Without Increasing the Antenna Aperture

Gaofeng Shu, Nan Wang, Wentao Wang, Yunkai Deng, *Member, IEEE*, Yongwei Zhang, Heng Zhang, *Member, IEEE*, Ning Li, *Member, IEEE*, and Robert Wang, *Senior Member, IEEE*

***Abstract*— Synthetic aperture radar (SAR) is an advanced ground-observing remote sensing technology, and high-resolution wide-swath (HRWS) imaging has always been the goal of SAR. In general, an improved azimuth resolution requires a large pulse repetition frequency (PRF), resulting in high system requirements. To overcome this difficulty, azimuth multichannel technology has gradually developed, achieving HRWS imaging and decreasing the PRF by increasing the spatial sampling, i.e., increasing the number of antenna subapertures in the azimuth. This article proposes a theoretical architecture that generates multiple virtual receiving apertures in the azimuth rather than real apertures. The virtual receiving apertures are formed by multiplying the azimuth signals by linear phase histories provided by vortex beams carrying different orbital angular momentum (OAM) modes. Vortex beams with different OAM modes have different oblique phase wavefronts, so virtual receiving positions are generated in the along-track direction. This approach aims to reduce the PRF without increasing the azimuth real receiving aperture. Simulation results demonstrate the effectiveness and limitations of the method. Finally, to overcome the inherent limitations of the method, two possible implementation schemes are proposed.**

***Index Terms*— Antenna radiation patterns, azimuth multichannel, orbital angular momentum (OAM), pulse repetition frequency (PRF), synthetic aperture radar (SAR), vortex beams.**

I. Introduction

SYNTHETIC aperture radar (SAR) is an advanced earth observation radar that has the capability of high-resolution imaging, environmental monitoring, resource mapping, and moving targets detection and is independent of weather conditions and sunlight illumination [1]. SAR has been greatly developed and widely used since its principle was discovered in the early 1950s [2], [3]. Currently, SAR has become an indispensable technology in the field of microwave imaging.

High-resolution wide-swath (HRWS) imaging has always been the goal of SAR systems in remote sensing applications [4]. There are at least three distinct SAR modes, stripmap SAR, spotlight SAR, and scan SAR [5], [6]. Spotlight SAR can achieve a relatively fine resolution but with noncontiguous spatial coverage, which is much smaller than that of stripmap SAR. On the other hand, scan SAR mode enables a wide swath but sacrifices the azimuth resolution. It seems that there is a tradeoff between azimuth resolution and swath area [7]. Taking stripmap SAR as an example, a higher azimuth resolution requires a wider Doppler bandwidth and thus needs a higher pulse repetition frequency (PRF) to alleviate azimuth ambiguities. However, the PRF should be low enough that the range swath width can be as large as possible without exhibiting range ambiguities [6]. In other words, the choice of the PRF is a compromise mainly between the azimuth ambiguity levels, range ambiguity level, and swath width, especially in the spaceborne case.

However, it is difficult for traditional SAR systems to meet the increasing demands of higher resolution and wider swath. Fortunately, to address this dilemma, single-transmitter multiple-receiver technology, usually named azimuth multichannel SAR, has been considered to enable HRWS imaging [4], [7], [8]. In an azimuth multichannel SAR system, mutually displaced receiving apertures, which are distributed in the along-track direction, receive the backscattered signals simultaneously and independently. The additional spatial sampling allows the system to reduce the time sampling, i.e., to decrease the PRF and, thus, the Doppler spectrum aliases. Gebert *et al.* [7] introduced azimuth multichannel SAR systems and principles in detail and presented an algorithm to reconstruct the azimuth signal without any ambiguities from the multichannel aliased signals. The algorithm relies mathematically on generalized sampling expansion [9] and technically on digital beamforming (DBF) technology [7], [10], [11], a powerful technique to enhance the antenna performance for the receiving mode, which is considered to be able to improve the azimuth coverage and resolution simultaneously [7], [12]. A larger total antenna area, an increased data rate, and a higher

Manuscript received February 5, 2020; revised July 22, 2020 and December 23, 2020; accepted January 12, 2021. Date of publication March 2, 2021; date of current version December 6, 2021. This work was supported in part by the National Natural Key Research and Development Program of China under Contract 2017YFB0502700, and in part by the China Scholarship Council (CSC) under Grant 201904910832. *(Corresponding author: Robert Wang.)*

Gaofeng Shu and Yongwei Zhang are with the Department of Space Microwave Remote Sensing Systems, Aerospace Information Research Institute, Chinese Academy of Sciences, Beijing 100094, China, and also with the School of Electronic, Electrical and Communication Engineering, University of Chinese Academy of Sciences, Beijing 100039, China (e-mail: gaofeng.shu@foxmail.com).

Nan Wang, Wentao Wang, Yunkai Deng, Heng Zhang, and Robert Wang are with the Department of Space Microwave Remote Sensing Systems, Aerospace Information Research Institute, Chinese Academy of Sciences, Beijing 100094, China (e-mail: yuwang@mail.ie.ac.cn).

Ning Li is with the School of Computer and Information Engineering, Henan University, Kaifeng 475004, China.

Digital Object Identifier 10.1109/TGRS.2021.3053650

data processing capability are required to take advantage of the azimuth multichannel SAR system based on DBF [12].

Many published studies have studied HRWS SAR imaging, including system design [4], [11], imaging algorithms [7], [13]–[18], channel error estimation [19]–[21], and ambiguous suppression [22]–[24]. To the best of our knowledge, a few published research articles have focused on how to reduce the antenna aperture. In the azimuth multichannel SAR echo model, the received azimuth signals of each channel are approximately equivalent to time-delayed signals with regard to a monostatic azimuth response [7], which is usually called a referenced signal. The time-delayed signal can be considered as a multiplication of a linear phase term, related to the azimuth distance of the receiving channel, with the referenced signal after a binomial expansion. Inspired by this fact, if one multiplies the monostatic azimuth response by a linear phase function through DBF in a single-channel system, the signal equivalently received by an offset receiver in azimuth can be obtained. Next, if the multiplication is repeated with more different linear phase functions, signals similar to azimuth multichannel SAR signals are generated, resulting in a low PRF for the system without increasing the antenna aperture.

Multiple linear phase functions can be achieved with electromagnetic waves carrying orbital angular momentum (OAM), which are usually called OAM beams or vortex beams [25]. A vortex beam has a helical phase wavefront of $\exp(jL\varphi)$, where φ is the transverse azimuthal angle around the propagation direction and L is an integer indicating the OAM mode [26], [27]. The amplitude of a nonzero-mode OAM beam is doughnut-shaped, and its phase is linear around the beam axis and approximately linear along a straight trajectory in the main lobe, as shown in Section II-B.

For OAM-based radar imaging, the azimuth angle resolution of the targets can be achieved via spectral estimation method, such as a Fourier transform method or multiple signal classification (MUSIC) method [28]–[31]. On the other hand, the research of vortex EM waves in radio communication and radar fields has paved the way for its application in SAR imaging. For example, a novel 3-D SAR imaging method based on the vortex EM wave is proposed, but the third dimension, i.e., the azimuth angle, is also obtained via spectral estimation method [32]. Due to the amplitude and phase characteristics of the OAM beams, an extra amplitude and phase compensation is a necessary process in the imaging algorithm of the SAR imaging based on OAM waves [33]–[35]. Bu *et al.* [36] implemented the SAR imaging based on the OAM waves via a vehicle-borne experiment, in which only a part of the energy of the main lobe is used through a large incident angle.

In this article, a novel SAR imaging system that decreases the PRF performs like azimuth multichannel SAR but without increasing the antenna area is introduced with the help of OAM waves. For this purpose, first, all of the signals received by each of the antenna elements under a low-PRF system are stored. Second, each of these signals is multiplied by a phase weight. This approach is equivalent to receiving an echo by a phased array. The phase distribution of all of the antenna elements generates a vortex beam with its main lobe illuminating the swath. Then, the stored original signals can be multiplied by a series of phase distributions that generate vortex beams carrying different modes of OAM. The purpose of the step is to obtain multiple linear-phase-weighted signals along the azimuth, which is equivalent to azimuth multichannel SAR echoes as described previously. Finally, the traditional multichannel reconstruction algorithm [7], [16] is applied for imaging processing.

This article is organized as follows. Section II summarizes the basic signal model and reconstruction algorithm of the traditional azimuth multichannel SAR system and describes the properties of the linear phase in vortex beams. In Section III, the detailed concepts and approach are illustrated to show how the proposed system works for situations ranging from a simple OAM mode to complicated multiple OAM modes, followed by an introduction of the system design from the perspective of the wavefront. A series of 1-D and 2-D simulations of our signal model is presented in Section IV. Then, in Section V, the advantages and disadvantages are described, followed by alternative proposals that may be applied with the proposed system. Finally, Section VI draws the major conclusions and describes future work.

II. Basic Theory

In the following, the signal model of azimuth multichannel SAR is recalled briefly. An equivalent form of the signal is introduced to adopt a vortex pattern, which will show how the proposed system works as a multichannel SAR system.

A. Azimuth Multichannel SAR Signal

The general azimuth multichannel SAR geometry is shown in Fig. 1. For simplicity, three channels are considered as an example. The three rectangles in the azimuth represent three channels, i.e., three receivers (Rxs), which are numbered as indices. In general, all of the channels receive echoes in the receive window, and only channel 0 operates as a transmitter (Tx) in the transmit window and as a reference channel in this example. The distance between the ith channel and the reference channel is d_i and $d_0 = 0$ obviously. Let the SAR mode be a simple broadside stripmap mode and P be a point target on the ground within the swath, so the distances between P and Rxs are

$$r_i = \sqrt{r_0^2 + d_i^2} \approx r_0 + \frac{d_i^2}{2r_0} \tag{1}$$

where $r_0 = R_0$ is the minimum slant range between the target and the reference channel. The approximation is performed, given that $r_0 \gg d_i$ for all i in practice.

The monostatic azimuth response of a point-like target can be expressed as

$$\begin{aligned} s_0(\eta) &= \exp\left[-j\frac{4\pi}{\lambda}\sqrt{R_0^2 + (V_r\eta)^2}\right] \\ &\approx \exp\left(-j\frac{4\pi R_0}{\lambda}\right)\exp\left(-j\frac{2\pi V_r^2}{\lambda R_0}\eta^2\right) \end{aligned} \tag{2}$$

where V_r is the velocity of the radar platform, λ is the carrier wavelength, and η is the azimuth time. The quadratic

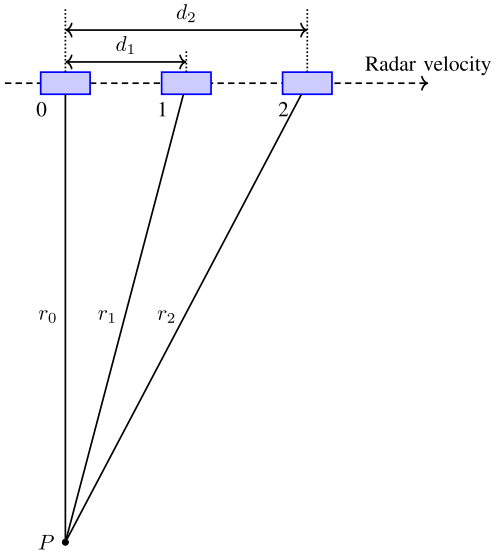

Fig. 1. General geometry of the azimuth multichannel SAR system. The blue filled rectangles are antennas with the number index shown on the left. The distances between each antenna and channel 0 are denoted by d_i, and the distances between the antennas and a point P on the ground are denoted by r_i, where $i = 0, 1, 2$.

approximation is justified by the fact that $V_r\eta \ll R_0$ in general. In addition, $K_a = -2\ V_r^2/\lambda R_0$ is the azimuth frequency modulated rate in this case.

For a given channel i, similarly, the azimuth response is

$$\begin{aligned} s_i(\eta) &= \exp\left[-j\frac{2\pi}{\lambda}\left(\sqrt{R_0^2+(V_r\eta)^2}+\sqrt{R_0^2+(V_r\eta-d_i)^2}\right)\right] \\ &\approx \exp\left(-j\frac{4\pi R_0}{\lambda}\right)\exp\left(-j\frac{\pi d_i^2}{2\lambda R_0}\right) \\ &\quad\cdot\exp\left[j\pi K_a\left(\eta-\frac{d_i}{2V_r}\right)^2\right] \\ &= s_0(\eta-\eta_i)\cdot\exp(j\varphi_i) \end{aligned} \tag{3}$$

which is cited from [7] with only a slight notation change. $\eta_i = d_i/2V_r$ and $\varphi_i = -\pi d_i^2/2\lambda R_0$ are a time delay and a constant phase shift, respectively. Compared with the monostatic case (2), the effective phase center position of the multichannel SAR azimuth response is exactly at the middle of Tx and Rx.

According to signal processing techniques or Fourier analysis, the azimuth multichannel response (3) is a time-delayed signal of the monostatic response; hence, the transfer function in the Doppler frequency domain between the multichannel and monostatic is written as

$$\begin{aligned} H_i(f_\eta) &= \exp\left(-j\frac{\pi d_i^2}{2\lambda R_0}\right)\cdot\exp\left(-j2\pi\frac{d_i}{2V_r}f_\eta\right) \\ &= \exp\left(-j2\pi\eta_i f_\eta\right)\cdot\exp(j\varphi_i) \end{aligned} \tag{4}$$

where f_η is the Doppler frequency. As a result, the multichannel impulse response of channel i can be expressed as

$$S_i(f_\eta) = S_0(f_\eta)\cdot H_i(f_\eta) \tag{5}$$

where $S_0(f_\eta)$ is the monostatic impulse response and $H_i(f_\eta)$ can be regarded as a linear system. Assuming that the number of channels is M, M received signals $s_i(\eta)$ are digitally sampled at a sample frequency of PRF. The sampled signals are denoted as $g_i(n/\mathrm{PRF})$, where n is the sample. According to [9], $s_0(\eta)$ is uniquely determined in terms of the samples $g_i(n/\mathrm{PRF})$ of M linear systems with input $s_0(\eta)$, sampled at $1/M$ the Nyquist rate, i.e., PRF $= B_a/M$, where B_a is the Doppler bandwidth.

A compact characterization of the whole system is then given by the matrix $\boldsymbol{H}(f)$ [7], which is considered as a system transfer matrix

$$\boldsymbol{H}(f_\eta) = \begin{bmatrix} H_1(f_\eta) & \cdots & H_M(f_\eta) \\ H_1(f_\eta+\sigma) & \cdots & H_M(f_\eta+\sigma) \\ \vdots & \ddots & \vdots \\ H_1(f_\eta+(M-1)\cdot\sigma) & \cdots & H_M(f_\eta+(M-1)\cdot\sigma) \end{bmatrix} \tag{6}$$

where $\sigma =$ PRF to shorten the formula. Then, the corresponding reconstruction filter is

$$\boldsymbol{P}(f_\eta) = M\cdot\boldsymbol{H}^{-1}(f_\eta). \tag{7}$$

By applying the reconstruction filter (7), the monostatic impulse response $S_0(f_\eta)$ can be reconstructed by M channels of echoes that are undersampled by PRF $= B_a/M$.

Now, let us expand $(\eta-\eta_i)^2$ in (3) and obtain

$$\begin{aligned} s_i(\eta) &\approx \exp\left(-j\frac{4\pi R_0}{\lambda}\right)\exp\left(-j\frac{\pi d_i^2}{2\lambda R_0}\right) \\ &\quad\cdot\exp\left[j\pi K_a\eta^2 - j2\pi K_a\frac{d_i}{2V_r}\eta - j\frac{\pi d_i^2}{2\lambda R_0}\right] \\ &= s_0(\eta)\cdot\exp(-j2\pi K_a\eta_i\eta)\exp(j2\varphi_i). \end{aligned} \tag{8}$$

From (8), the signal received by channel i can be regarded as the monostatic impulse response $s_0(\eta)$ multiplied by a linear phase in the time domain and a constant phase term. Undoubtedly, M undersampled signals in a form such as (8) can be reconstructed by the filter (7) because (3) and (8) are mathematically equivalent. It is worth pondering what will happen if there is only one aperture but the echo is multiplied by a set of linear phase terms. This question inspires all of the ideas about this article.

The range of the linear phase term in (8) in synthetic aperture time, i.e., target exposure time, is

$$\begin{aligned} \Delta\varphi_i &= -2\pi K_a\eta_i T_s \\ &= 2\pi\cdot\frac{2V_r^2}{\lambda R_0}\cdot\frac{d_i}{2V_r}\cdot\frac{\lambda R_0}{DV_r} \\ &= 2\pi\frac{d_i}{D} \end{aligned} \tag{9}$$

where $T_s = \lambda R_0/DV_r$ is the synthetic aperture time [6] and D is the azimuth aperture of Tx.

B. Vortex SAR Model

The vortex beam, which carries OAM, has a helical phase wavefront of $\exp(jL\varphi)$ around its beam center. There are many methods to generate OAM beams in the radio domain, but phased arrays such as uniform circular array (UCA) are

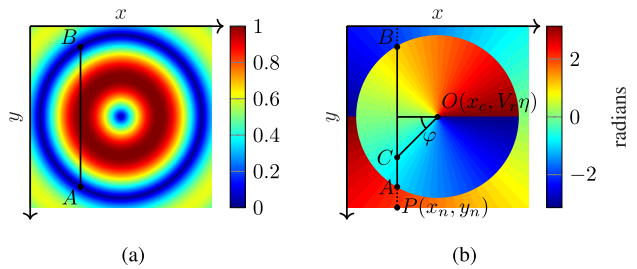

Fig. 2. Vortex pattern generated by a UCA with OAM mode $L = 1$. (a) Amplitude and (b) phase pattern in the plane perpendicular to the propagation direction z. O is the beam center, and P is a hypothetical point target. A and B indicate where point P enters and leaves the main lobe of the beam, respectively. C is the waypoint.

the most common method due to their intuition and convenience [26], [27], [37]. Fig. 2 shows the amplitude and phase pattern generated by a UCA with OAM mode $L = 1$, which is exhibited from the rotational phase front. The phase is linear with regard to the rotational azimuth angle naturally from the source.

Now, if a UCA, mounted on an SAR platform with a look angle $\alpha = 0$ relative to the vertical, generates a vortex beam, the radar footprint can also be shown in Fig. 2. Let the radar fly along the y-direction, i.e., from top to bottom in Fig. 2, and then, x and y are the range and azimuth directions, respectively. Assuming that the beam center is denoted as $O(x_c, V_r\eta)$ at a particular azimuth time η and a hypothetical point target is located at $P(x_n, y_n)$, the radar platform moves along the $+y$-direction, which can be considered as P traveling from A through C to B along the $-y$-direction with respect to the radar platform to experience the whole amplitude and phase of the main lobe of the vortex beam. C is a waypoint on the closed line segment $\overline{AB}$, and φ is the azimuth angle with respect to O. If P arrives at C, and then, the azimuth angle is

$$\varphi_C = \arctan\left(\frac{y_n - V_r\eta}{x_c - x_n}\right). \tag{10}$$

The ring shape of the amplitude becomes larger with increasing L or a decreasing antenna aperture D [38]. To guarantee that the point P is always in the main lobe, as shown in Fig. 2(a), the beam center must point farther away from P. In other words, x_c varies with L and D, denoted as $x_c(L, D)$, and there is an offset distance between $x_c(L, D)$ and x_n. In practice, the look angle $\alpha \neq 0$, so the phase history of P traveling in the main lobe of a vortex beam with OAM mode L is

$$\varphi(L, \eta) = -L \arctan\left[\frac{V_r\eta}{(x_c(L, D) - x_n)\cos\alpha}\right]. \tag{11}$$

Because the phase history of the point within a range gate along the y-direction is the same, it is reasonable to assume $y_n = 0$. The denominator and numerator within square brackets in (11) represent the process of the synthetic aperture and the offset distance between the vortex beam center and the maximum radiation on the ground, respectively. It is convenient to denote "AOR" to indicate the ratio of synthetic aperture to the offset distance, i.e.,

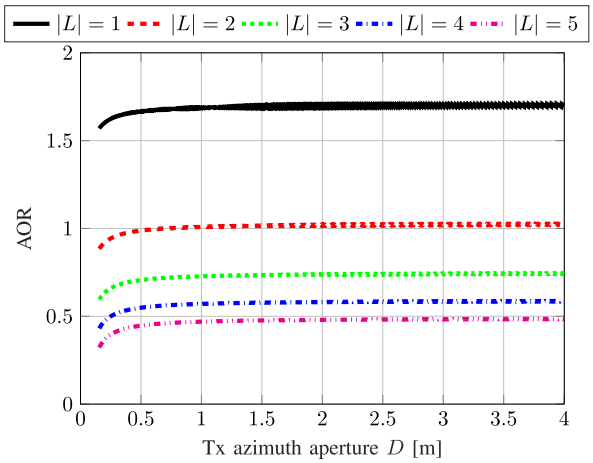

Fig. 3. AOR vs. Tx azimuth aperture D and OAM mode $|L|$. The black solid, red dashed, green dotted, blue dash-dotted, and magenta dash-dotted dotted lines represent $|L| = 1, 2, 3, 4$, and 5, respectively.

$$\text{AOR} = \frac{V_r T_s}{(x_c(L, D) - x_n)\cos\alpha}. \tag{12}$$

Remember that the synthetic aperture time in the proposed system is only for the OAM mode $L = 0$ (see Section III-A), which means that T_s does not depend on L. The relationship between AOR and D with L is shown in Fig. 3. It can be seen that AOR increases as D increases in the domain of $D < 0.5$ m and AOR becomes almost flat in the domain of $D > 0.5$ m, so D in $x_c(L, D)$ is often omitted, especially for a fixed D in an SAR system. In addition, with the increasing $|L|$, AOR decreases and AOR < 1 when $|L| > 2$ in particular.

Under the condition of AOR < 1, the Taylor expansion of (11) is expressed as

$$\varphi(L, \eta) = -L\frac{\text{AOR}}{T_s}\eta + L\frac{\text{AOR}^3}{3T_s^3}\eta^3 - \cdots. \tag{13}$$

Let

$$F_L = \frac{L \cdot \text{AOR}}{2\pi T_s} \tag{14}$$

$$A_L = \frac{L \cdot \text{AOR}^3}{\pi T_s^3} \tag{15}$$

where 2π and π in the denominator are normalization factors to maintain a consistent dimension. F_L and A_L are strongly related to the OAM mode L for a fixed Tx aperture D, and Fig. 4 shows their relationships. In the domain of $|L| < 20$, F_L increases with increasing L, and the gradient gradually decreases. When $|L| > 20$, F_L decreases as L increases, and the values of F_L corresponding to two adjacent values of L are very close. This is reasonable because AOR decreases as L increases, which slows down the increase in F_L. For most values of L, the corresponding value of A_L tends to zero, except for some small $|L|$. A_L decreases rapidly when L increases from 1 to 10. In addition, F_L and A_L are both odd functions with respect to L.

Substituting (14) and (15) into (13), we obtain

$$\varphi(L, \eta) \approx -2\pi F_L\eta + \frac{\pi}{3}A_L\eta^3. \tag{16}$$

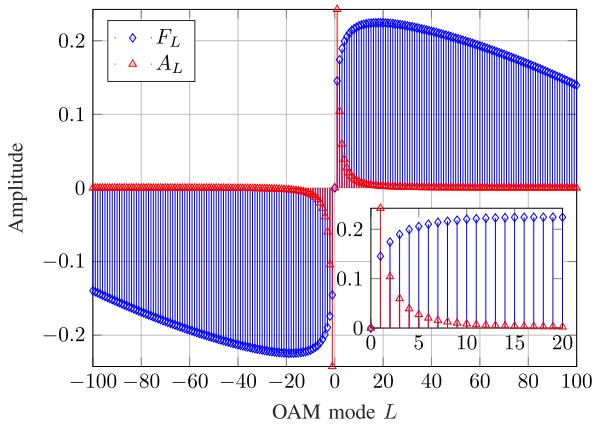

Fig. 4. The relationships between F_L, A_L and L in the case of $D = 2$. The blue stems with diamonds represent F_L, and the red stems with triangles represent A_L. The small axis inside shows the data limited within $L \in [0, 20]$.

For a fixed D, if the appropriate L, such as $|L| > 2$, is chosen, $A_L \propto \text{AOR}^3$ is small enouth so that $\varphi(L, \eta)$ becomes approximately linear and the gradient ultimately depends on L. Therefore, if the SAR system transmits the ordinary beam (i.e., $L = 0$) and receives the returned echoes by a vortex beam with an OAM mode $L \neq 0$ or $|L| > 2$ discussed previously, the azimuth response becomes

$$\begin{aligned} s_L(\eta) &= s_0(\eta) \cdot \exp[j\varphi(L, \eta)] \approx s_0(\eta) \cdot \exp[-j2\pi F_L \eta] \\ &= s_0\left(\eta - \frac{F_L}{K_a}\right) \exp\left(-j\pi \frac{F_L^2}{K_a}\right) \\ &= s_0(\eta - \eta_L) \exp(-j\varphi_L) \end{aligned} \tag{17}$$

where

$$\eta_L = \frac{F_L}{K_a} \tag{18}$$

$$\varphi_L = \frac{\pi F_L^2}{K_a}. \tag{19}$$

Compared (17) with (3), it is found that the proposed vortex SAR system echo is equivalent to the azimuth multichannel subaperture echo, with only a constant phase difference. Therefore, the same processing algorithm can be used. Recalling (4) and (8), the transfer function of the vortex SAR model can be written as

$$H_L(f_\eta) = \exp(-j2\pi \eta_L f_\eta) \cdot \exp(-j\varphi_L). \tag{20}$$

The slope of the linear transfer function is determined by η_L or F_L, which is very important for the signal reconstruction in the proposed system. Equations (17) and (20) are the azimuth response and the corresponding transfer function for just one OAM mode L, respectively, which resemble those of one channel signal in the azimuth multichannel system. If multiple OAM modes are applied, it can be seen from (17) that multiple azimuth response echoes that vary with L will be obtained, just like the azimuth multichannel echoes of each subchannel. Since their mathematical expressions are equivalent as well as the reconstruction filters, the proposed system can reduce the system PRF as well as the azimuth multichannel system.

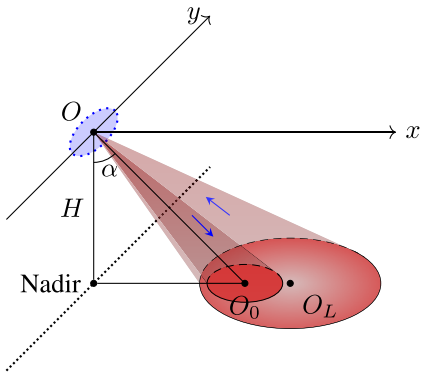

Fig. 5. General geometry of vortex SAR. A radar platform flies along the y-direction and works in broadside stripmap mode with altitude H and look angle α. A vortex antenna is mounted on the radar platform, transmitting OAM mode $L = 0$ and receiving OAM mode $L \neq 0$ with an offset distance $\overline{O_0\ O_L}$ along the range.

III. Proposed Vortex SAR System

In this section, our proposed vortex SAR system based on theories discussed in Section II is introduced in two cases. Some comparisons between the vortex SAR system and azimuth multichannel SAR system are presented. At the end of this section, a wavefront perspective is presented for a better understanding.

A. System Design

1) One OAM Mode: Fig. 5 shows the geometry of the proposed vortex SAR geometry. The axes x and y represent the direction of the ground range and azimuth, respectively. A radar platform with a mounted vortex antenna, such as a UCA, flies along the $+y$-direction at a velocity of V_r and an altitude of H. The vertical look angle is α, and the squint angle is 0. The transmitting beam is an ordinate beam, i.e., OAM mode $L = 0$, whereas the receiving beam is a vortex beam with $L \neq 0$. The centers of both beams hitting on the ground are denoted by O_0 and O_L, respectively, with subscripts of zero and the OAM mode. If the antenna is fixed on the radar platform, O_0 and O_L are generally coincident. The returned echoes are very weak, although the transmitting beam is concentrated with high power, because there is a null power region around the beam axis of the receiving beam [26], [38]. It is not difficult to collimate the main lobe to cover the same area as the transmitting beam via applying phased array techniques, as shown in Fig. 5. The straight distance between O_0 and O_L on the ground is the offset distance mentioned in Section II-B, i.e., the denominator of AOR.

The transmitted pulses radiate from Tx to the ground with the transmitting pattern of OAM mode $L = 0$. In the interval between two successive pulses, a receiving pattern of OAM mode $L \neq 0$ is controlled by DBF techniques. The footprint of the receiving pattern is much wider than that of the transmitting pattern. Fortunately, the energy outside the footprint of the transmitting pattern is low enough with the help of beam shaping and sidelobe suppression techniques. The synthetic antenna pattern, the product of the transmitting pattern and receiving pattern, is shown in Fig. 6, with OAM modes $L = 0$ and $L = 3$.

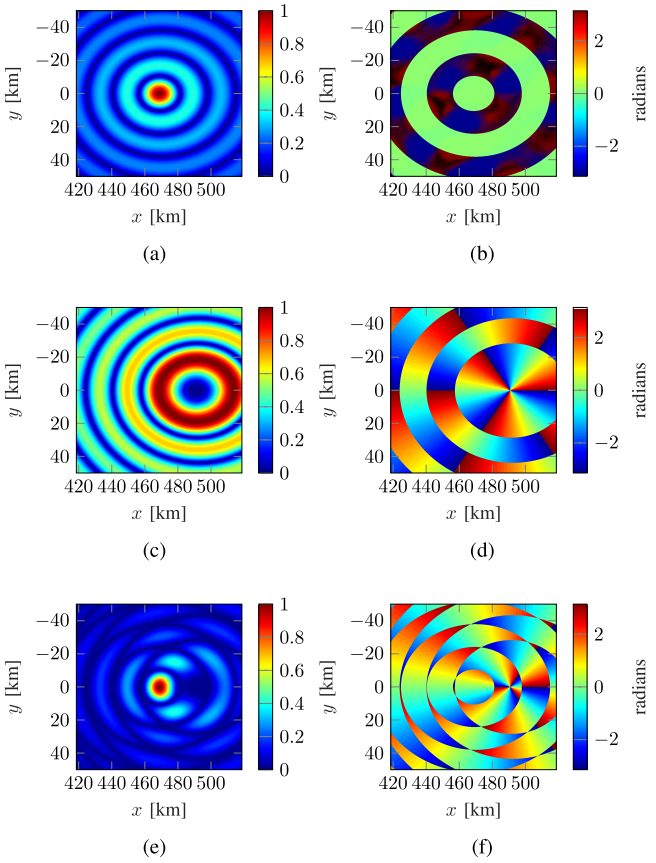

Fig. 6. Example of a synthetic antenna pattern. (a), (c), and (e) and (b), (d), and (f) Amplitude and phase pattern on the ground, respectively, generated by a UCA mounted on a radar platform. The top row [(a) and (b)] and middle row [(c) and (d)] are antenna patterns of vortex beams with OAM modes $L = 0$ and $L = 3$, respectively. The bottom row [(e) and (f)] are synthetic antenna patterns.

As shown in Fig. 6(e) and (f), the main lobe of the synthetic pattern is slightly smaller and the energy of the sidelobes of the synthetic pattern is much weaker than those of the $L = 0$ mode. All echoes come from the reflection of the targets in the main lobe of the synthetic pattern, which is collimated at a small area on the ground. It is noticeable that the phase of the synthetic pattern is significantly different from that of $L = 0$ and $L = 3$. It can be seen that the phase in the main lobe is identical to that of $L = 3$, approximately linear along the azimuth, as derived in Section II-B previously and exactly as desired.

Notably, the signal received by the designed receiving pattern has the form of (17). Compared with the azimuth multichannel signal (8), it is equivalent that a virtual Rx separated along the azimuth from the Tx receives the echoes. Detailed information about the virtual Rx is described in Section III-B from the perspective of the wavefront.

The difficulties and disadvantages of this system include element-level DBF technology, low energy efficiency, and only one offset virtual channel. A single Tx and only one offset Rx cannot produce any additional new information. The system that brings more virtual offset Rxs, such as an azimuth multichannel system, becomes necessary.

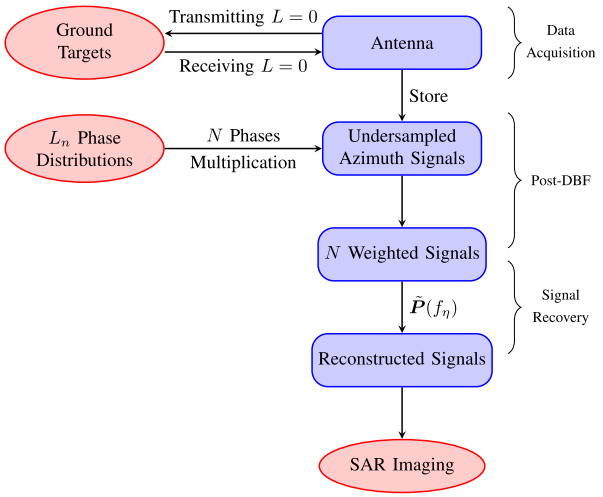

Fig. 7. Flow diagram of the proposed SAR system.

2) Multiple OAM Modes: During a receiving window time, the receiving pattern should be only one OAM mode or the received signals will be unclear, which leads to just one virtual offset Rx channel. Multiple virtual offset Rxs need multiple receiving OAM modes, which cannot be realized in real time within the receiving time. Therefore, an intuitive idea is to store the echoes received by each receiving antenna element and then multiply each signal of the receiving antenna element by a set of phases to form different vortex patterns with the corresponding OAM modes. The operation of phase multiplication after data acquisition can be regarded as post-DBF processing, which is more important than the idea of providing a linear phase with vortex beams in this proposed vortex SAR system. A schematic of the proposed system is shown in Fig. 7. The main steps of the system are divided into data acquisition, post-DBF, and signal recovery. Post-DBF is a distinct, unique, and indispensable method in this proposed system.

As shown in Fig. 7, first, the UCA as a Tx transmits a chirp pulse with transmitting pattern $L = 0$; then, the same UCA as an Rx with receiving pattern $L = 0$ receives the signals returned from ground targets and stores the echoes by each antenna element. Second, choose N proper vortex OAM modes satisfying the condition AOR < 1, such as $L_n, n = 1, 2, \cdots N$ modes. The PRF of the system is set to $1/N$ the Nyquist rate so that N different undersampled azimuth responses are obtained, which are similar to the data acquisition of the azimuth multichannel system. Third, a signal recovery algorithm is applied to reconstruct the aliased signals. Compared with (6), (7), and (20), we can obtain a similar result for the system transfer matrix

$$\tilde{\boldsymbol{H}}(f_\eta) = \begin{bmatrix} H_{L_1}(f_\eta) & \cdots & H_{L_N}(f_\eta) \\ H_{L_1}(f_\eta + \sigma) & \cdots & H_{L_N}(f_\eta + \sigma) \\ \vdots & \ddots & \vdots \\ H_{L_1}(f_\eta + (N-1)\cdot\sigma) & \cdots & H_{L_N}(f_\eta + (N-1)\cdot\sigma) \end{bmatrix} \tag{21}$$

where $\sigma = \text{PRF}$ for simplicity and the corresponding reconstruction filter is

$$\tilde{\boldsymbol{P}}(f_\eta) = N \cdot \tilde{\boldsymbol{H}}^{-1}(f_\eta) \tag{22}$$

if $\tilde{\boldsymbol{H}}(f_\eta)$ is invertible. The condition for $\tilde{\boldsymbol{H}}(f_\eta)$ to be invertible is written as follows:

$$F_{L_i} \neq F_{L_j} + \frac{kN}{T_s}, \text{ for all } i \neq j \tag{23}$$

where k is an integer. Equation (23) is derived in detail in the Appendix. The last step is the standard SAR imaging process, which is not the topic of this article.

From the above discussion, the proposed SAR system receives and stores the azimuth undersampled echoes through a single aperture and then performs multiple-phase multiplication operations to form "multichannel" data, followed by applying a similar filter reconstruction algorithm to obtain an unambiguous SAR echo signal. In the whole process, the antenna aperture does not increase, but the PRF can be reduced. The difficulty in the implementation lies in the element-level DBF technology and high data storage or data transmission requirements.

3) Comparisons With the Azimuth Multichannel SAR System: The azimuth multichannel system forms multiple linear systems because multiple real apertures are placed along the azimuth direction so that they can store the echoes of each channel. However, our proposed vortex SAR system has only one real aperture but many equivalent virtual apertures, which is an essential distinctness.

Since the proposed system essentially amounts to an azimuth multichannel system, the equivalent virtual Rx position d_L for a particular OAM mode L can be obtained from (18)

$$\begin{aligned} d_L &= 2V_r\eta_L = 2V_r \cdot \frac{L \cdot \text{AOR}}{2\pi T_s} \cdot \left(-\frac{\lambda R_0}{2V_r^2}\right) \\ &= -\frac{L \cdot \text{AOR}}{2\pi \frac{\lambda R_0}{DV_r}} \cdot \frac{\lambda R_0}{V_r} = -\frac{L \cdot \text{AOR}}{2\pi} D. \end{aligned} \tag{24}$$

From (24), it can be seen that for different L, different d_L can be obtained, which means that if multiple OAM modes are applied to the proposed system, a series of virtual receiving antennas can be formed, i.e., the equivalent echo of each subaperture in the azimuth multichannel SAR system can be obtained.

The range of the linear phase varying in a synthetic aperture time similar to (9) is expressed as

$$\Delta\varphi_L = 2\pi \frac{d_L}{D} = -L \cdot \text{AOR}. \tag{25}$$

The time delay and constant phase term in the equivalent transfer function can be rewritten as

$$\eta_L = \frac{F_L}{K_a} = \frac{d_L}{2V_r} = -\frac{L \cdot \text{AOR}}{2\pi} \cdot \frac{D}{2V_r} \tag{26}$$

$$\varphi_L = \frac{\pi F_L^2}{K_a} = -\frac{\pi d_L^2}{2\lambda R_0}. \tag{27}$$

Table I shows some parameters for a comparison of azimuth multichannel SAR system and the proposed vortex multi-OAM-mode SAR system. For the proposed system, $\Delta\varphi_L = -L \cdot \text{AOR}$ is a very important parameter because all other parameters are related to this parameter. $\Delta\varphi_L$ and d_L are not proportional to L because AOR varies with L. Therefore, the positions of the virtual Rxs are nonuniform. Fortunately, research on nonuniform azimuth multichannel is well developed [16], [18], and its reconstruction algorithm can be used directly for the proposed system. It is important to note that the constant phase in the transfer function differs from that of the azimuth multichannel by a negative sign, and the constant phase is usually very small.

TABLE I

SOME PARAMETERS OF THE AZIMUTH MULTICHANNEL SAR SYSTEM AND THE PROPOSED VORTEX MULTI-OAM-MODE SAR SYSTEM

	AMC[1]	VMM[2]
Equivalent Rx position from the Tx (d_i or d_L)	d_i	$-\frac{L \cdot \text{AOR}}{2\pi} D$
Range of the linear phase term ($\Delta\varphi_i$ or $\Delta\varphi_L$)	$2\pi \frac{d_i}{D}$	$-L \cdot \text{AOR}$
Equivalent time delay (η_i or η_L)	$\frac{d_i}{2V_r}$	$-\frac{L \cdot \text{AOR}}{2\pi} \frac{D}{2V_r}$
Equivalent constant phase (φ_i or φ_L)	$-\frac{\pi d_i^2}{2\lambda R_0}$	$-\frac{\pi d_L^2}{2\lambda R_0}$
Equivalent transfer function ($H_i(f_\eta)$ or $H_L(f_\eta)$)	$\mathrm{e}^{-\mathrm{j}2\pi\eta_i f_\eta}\, \mathrm{e}^{\mathrm{j}\varphi_i}$	$\mathrm{e}^{-\mathrm{j}2\pi\eta_L f_\eta}\, \mathrm{e}^{-\mathrm{j}\varphi_L}$

[1] Abbreviation for the azimith multichannel SAR system.
[2] Abbreviation for the vortex multi-OAM-mode SAR system.

In the proposed system, a significant feature is that the linear phase function along the azimuth in the main lobe slightly varies with the range gate due to the space-varying distribution of the phase of vortex beams, which can be seen from Fig. 6(f). This characteristic results in the requirement of different filters for targets located in different range gates to reconstruct signals.

B. Wavefront Perspective

The discovery of the virtual aperture can be studied from a more intuitive perspective, i.e., the perspective of the wavefront. Fig. 8 shows a schematic explaining the virtual aperture from the perspective of the wavefront. A real aperture antenna with an azimuth length of D mounted on an SAR platform flies along the y-direction at a velocity of V_r. The beam generated by the real aperture illuminates the ground with minimum slant range R_0, so the synthetic aperture is expressed $L_s = \lambda R_0 / D$.

As described in Section III-A1, the receiving pattern is a range-offset vortex pattern, so that the phase history of the azimuth is multiplied by a linear phase. Regarding the synthetic aperture as a Huygens source, a linear phase along a source results in a slant wavefront, the yellow line shown in Fig. 8; thus, the beam points in the direction perpendicular to the wavefront. A linear phase distribution along the sources is also the principle behind a phased array steering a beam of radio waves to a different direction [39].

The real aperture antenna receives the beam with a slant wavefront, which can be regarded as the virtual aperture at an offset position receiving a beam with a plane wavefront. The

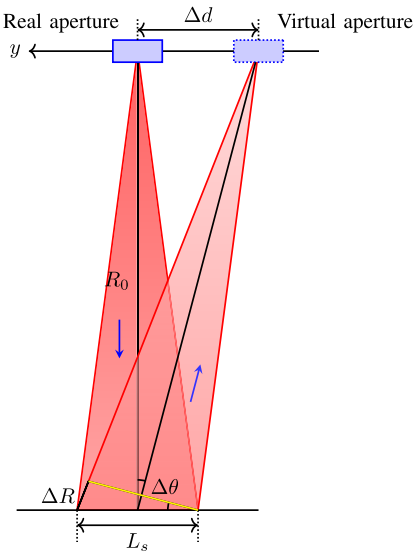

Fig. 8. Schematic of the virtual aperture from the perspective of the wavefront. The SAR platform with a real aperture, indicated by the blue solid filled rectangle, moves along the y-direction. The blue dashed filled rectangle is the virtual aperture separated from the real aperture by Δd. The minimum slant range is R_0 and the synthetic aperture length is L_s. ΔR is the wave path difference caused by the linear phase, and $\Delta\theta$ is the angle between the real aperture and the virtual aperture. The yellow line represents the wavefront of the reflected wave.

offset distance between the real aperture and virtual aperture is determined by the slope of the wavefront, and the latter is determined by the change in the phase in synthetic aperture, which is assumed to be $\Delta\varphi$. The wave path difference between both ends of synthetic aperture can then be written as

$$\Delta R = \Delta\varphi \cdot \frac{\lambda}{2\pi}. \tag{28}$$

Compared to L_s, ΔR is very small so that

$$\frac{\Delta d}{R_0} \approx \Delta\theta \approx \frac{\Delta R}{L_s} \tag{29}$$

and thus

$$\Delta d \approx R_0 \cdot \Delta\varphi \frac{\lambda}{2\pi} \cdot \frac{D}{\lambda R_0} = \frac{\Delta\varphi}{2\pi} D \tag{30}$$

which is consistent with (9) and (25). According to (30), the position of the virtual aperture is proportional to $\Delta\varphi$. For a fixed L, $\Delta\varphi_L = -L \cdot \mathrm{AOR}$ as shown in Table I.

The proposed system can be organized as follows.

1) Globally choose an appropriate number of L, i.e., an appropriate PRF for the system.
2) Transmit the beam with OAM mode $L = 0$, receive with the pattern for the OAM mode $L = 0$, and store all of the signals received by every element of the antenna.
3) Weight every signal by a particular phase according to the phase distribution to generate vortex OAM mode L. Different values of L produce different values of $\Delta\varphi$, thus producing different positions d_L and different transfer matrices.
4) Reconstruct the signal based on the reconstruction filter, i.e., an inversion of the transfer matrix.

IV. Simulation Results

In the following, a proof-of-concept SAR point-like target simulation is illustrated to show the ability to decrease the PRF by the proposed system above. Both 1-D and 2-D simulations are presented.

A. Simulation Parameters

First, the choice of L must be emphasized because it is related to the feasibility of the proposed system. In azimuth multichannel systems, if the equivalent spatial sampling positions are coincident, the signal reconstruction will fail. This is because the coincident spatial sampling positions cause the system transfer matrix to be singular and noninvertible [7]. To avoid this situation, we must choose the appropriate L carefully.

1) L determines the vortex antenna pattern and therefore determines the history of the azimuth phase. To alleviate the effect of the higher order phase in (13) on the imaging focus, AOR must be small enough, so L must be large enough. As shown in Fig. 3
$$|L| > 2. \tag{31}$$
2) On the other hand, if F_{L_i} and F_{L_j} are equal or close to each other, the system transfer matrix will be singular or the condition number of the matrix will be large; thus, the signal reconstruction will fail or achieve poor results. Therefore, it can be seen from Fig. 4 that the range of L is in a very limited domain.
3) For the generation of the vortex beams, a larger L requires more antenna elements [26], for example, N_{ant} elements of a UCA, i.e.,
$$|L| < \frac{N_{\mathrm{ant}}}{2}. \tag{32}$$

Based on the above discussion, we choose $L = 0, 9$, $L = -9, 0, 9$, $L = -20, -9, 9, 20$, and $L = -20, -9, 0, 9, 20$ to simulate two-, three-, four-, and five-OAM-mode SAR imaging, respectively. The other parameters are shown in Table II. The antenna aperture in the azimuth is $D = 2$ m, so the azimuth resolution in theory is

$$\rho_a \approx \frac{D}{2} = 1 \text{ m}. \tag{33}$$

B. 1D Simulation

A point target is positioned at the transmitting beam center. The scene size in the azimuth is chosen to be large enough to accommodate the synthetic aperture on the ground. The conventional azimuth echo undersampled at PRF $= O_s B_a / N$ is weighted by N phase distributions to implement a receiving echo using a vortex beam with different OAM modes. Then, a signal reconstruction algorithm similar to the azimuth multichannel reconstruction algorithm is performed to recover the aliased signal. Fig. 9 shows the reconstruction signal spectrum and the focusing of the point target in $N = 2, 3, 4, 5$ cases.

From Fig. 9(a)–(d), it can be seen that the aliased signals can be reconstructed by the reception of vortex beams with two and three modes such that the imaging quality parameters,

TABLE II

SIMULATION PARAMETERS FOR VORTEX MULTI-OAM-MODE SAR SYSTEM

Parameter	Symbol	Value
Carrier frequency	f_c	9.65 GHz
Orbit height	H	750 km
Look angle	α	32°
Squint angle	θ_{sq}	0°
Radar velocity	V_r	7400 m/s
Antenna aperture in the azimuth	D	2 m
Number of OAM modes	N	2, 3, 4, or 5
OAM modes	L	(0, 9), (-9, 0, 9), (-20, -9, 9, 20), (-20, -9, 0, 9, 20)
Doppler bandwidth	B_a	7400 Hz
Oversampling factor	O_s	1.3
Pulse repetition frequency	PRF	$O_s B_a / N$

TABLE III

CONDITION NUMBER OF THE TRANSFER MATRIX OF THE SYSTEM

Number of OAM modes	OAM modes	Condition number
2	$0, 9$	2.291
3	$-9, 0, 9$	5.165
4	$-20, -9, 9, 20$	332.325
5	$-20, -9, 0, 9, 20$	2418.862

the impulse response width (IRW), the peak sidelobe ratio (PSLR), and the integrated sidelobe ratio (ISLR), highly agree with the standard sinc-like function, of which the IRW, PSLR, and ISLR are approximately 1, -13.26 dB, and -10 dB, respectively. It is notable that the IRW value defines the point resolution, which agrees with the theoretical value given by (33).

However, for the case of four modes in Fig. 9(e) and (f), the reconstructed signal spectrum starts to deteriorate. As a result, the point target is not as perfect as the previous two cases. The same deterioration occurs in the case of five modes in Fig. 9(g) and (h), and the problem is more severe. The signal spectrum has failed to reconstruct so that the PSLR and ISLR of the point target are very high, and thus, the point target fails to focus.

After the analysis, it is found that the failure of the signal spectrum reconstruction is due to the fact that $F_9 \approx 0.217$ and $F_{20} \approx 0.224$ are too close, which makes the slopes of the linear phase of the transfer functions almost equal, i.e., $-2\pi\eta_9 \approx 3.42 \times 10^{-4}$ and $-2\pi\eta_{20} \approx 3.53 \times 10^{-4}$, which leads to an approximate singularity of the system transfer matrix, due to the large condition numbers, as shown in Table III.

C. 2-D Simulation

For a better illustration of the phase history varying along the range gate, three point targets, denoted as A, B, and C, are equally spaced on the ground along the range direction. Point target B is positioned at the transmitting beam center, similar to the point target in Section IV-B. A and C are -1000 and 1000 m away from B along the range direction, respectively. Similar to the 1-D simulation, the system PRF is also set to PRF $= B_a/N$, where N is the number of vortex modes L. The 2-D simulation results are presented in Fig. 10.

For $N = 2$ and $N = 3$ in Fig. 10(a)–(d) and (e)–(h), the targets are well focused. However, for the case of $N = 4$ in 10(i)–(l), the targets start to defocus with increasing range. For the case of $N = 5$, these point targets are defocused in the azimuth, which becomes more severe as the distance increases.

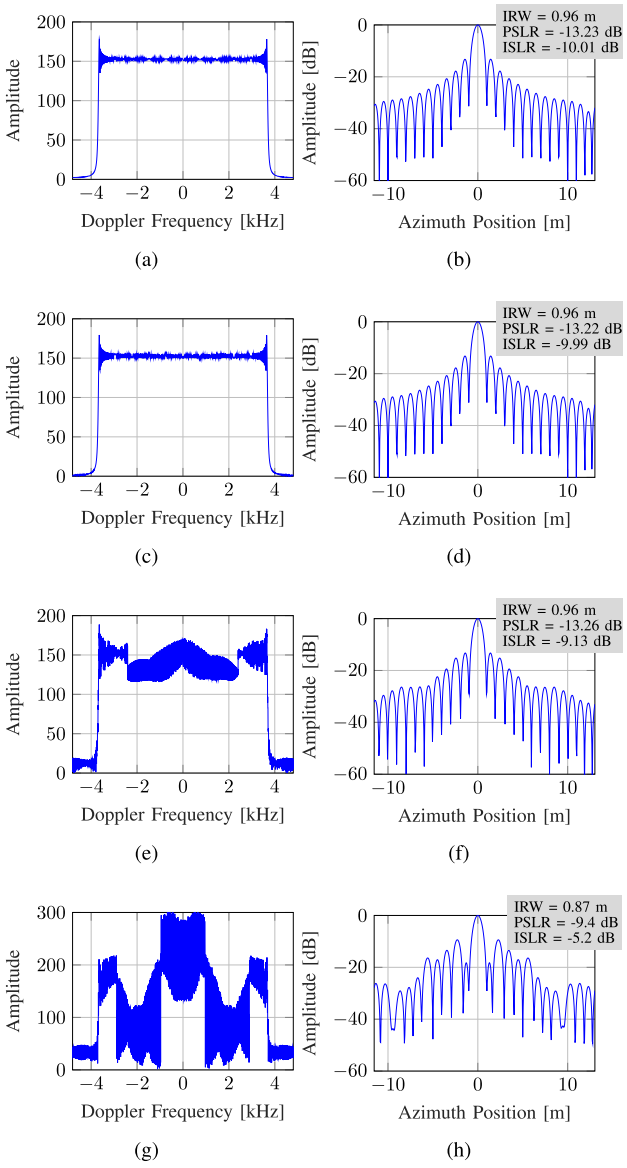

Fig. 9. Reconstruction signal spectrum (left column) and focusing of the point target (right column). Some of the imaging quality parameters, such as IRW, PSLR, and ISLR, are shown in the gray filled box aside the focusing point. The focusing point targets are reconstructed by 2 modes $L = 0, 9$ (a)(b), 3 modes $L = -9, 0, 9$ (c)(d), 4 modes $L = -20, -9, 9, 20$ (e)(f), and 5 modes $L = -20, -9, 0, 9, 20$ (g)(h).

The deterioration of the targets in the azimuth with increasing range is due to the fact that a larger distance corresponds to being closer to the vortex beam center and thus a higher order in the azimuth phase history. In addition, defocus becomes severe with increasing N, which is due to the approximate singularity of the reconstruction filter as mentioned before.

V. DISCUSSION

A. Advantages and Disadvantages

Based on the theoretical analysis and simulation results, compared with the azimuth multichannel SAR system, the

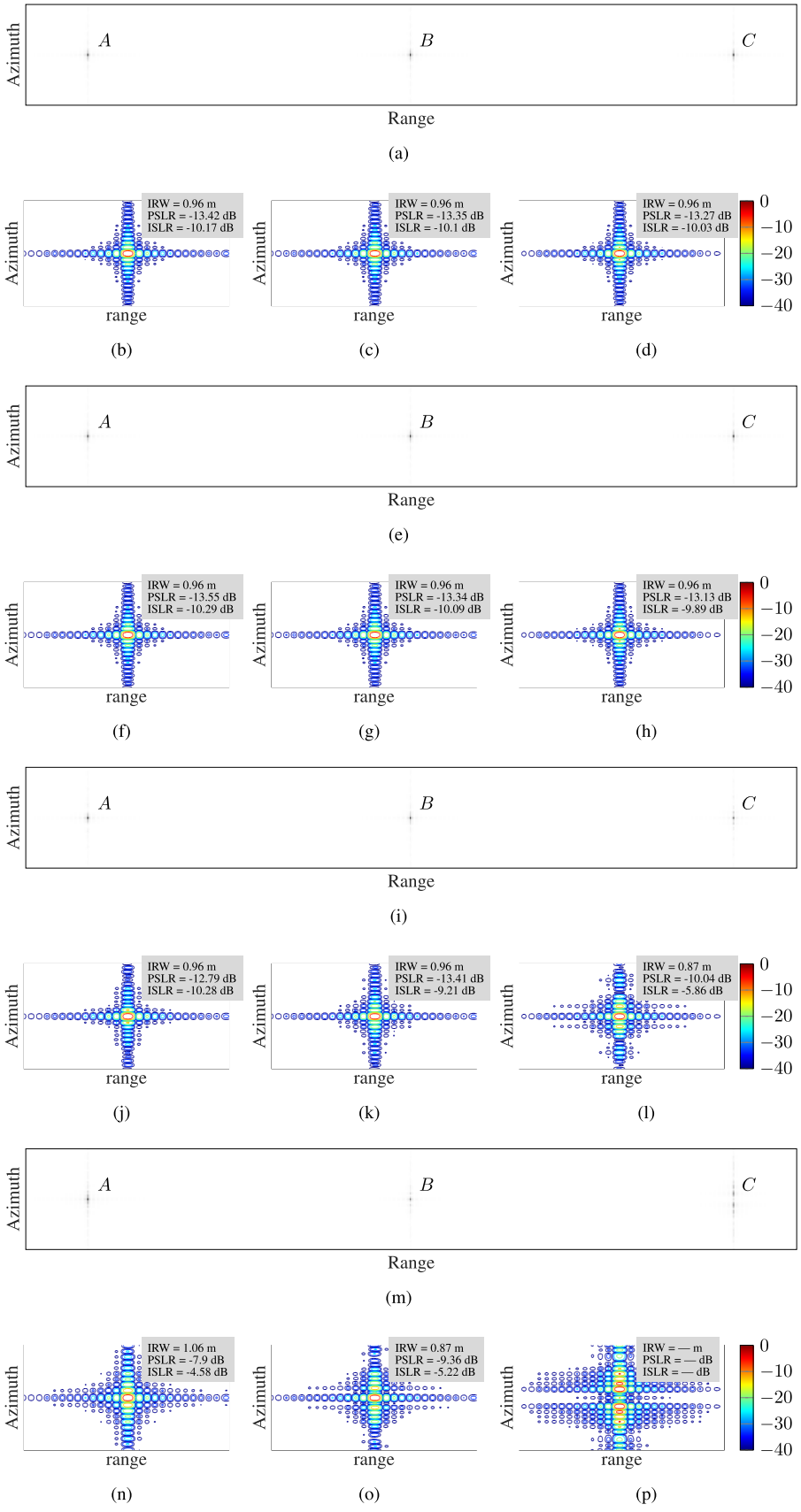

Fig. 10. Results of the 2-D simulations. (a), (e), (i), and (m) Compressed targets reconstructed by two modes $L = 0, 9$, three modes $L = -9, 0, 9$, four modes $L = -20, -9, 9, 20$, and five modes $L = -20, -9, 0, 9, 20$, respectively. (b), (c), and (d), (f), (g), and (h), (j), (k), and (l), and (n), (o), and (p) Contours of targets A, B, and C in (a), (e), (i), and (m) after an interpolation, respectively. The IRW, PSLR, and ISLR of the azimuth profiles are shown in the gray filled box aside the focusing point.

proposed system reduces the system PRF without increasing the antenna aperture. The swath is determined by only one antenna aperture, and the azimuth resolution is maintained at a low PRF. Regardless of other factors, the proposed system uses a single aperture to send and receive echoes, which achieves a wide swath, implements the focus on the targets, and reduces the high requirement for the PRF. This is the main advantage of the proposed system. It is noticed that the proposed system makes use of only one part of the ring shape of vortex beams, the part where the phase changes along azimuth. There is potential and flexibility in exploiting the other parts of vortex beams.

Any gains will definitely be achieved at the expense of other cost. For our purpose, DBF technology based on the element level is necessary to generate a vortex beam as a receiving pattern. It needs to store or transmit the data received by each antenna unit, which is very difficult. Compared with a conventional SAR system, the azimuth multichannel SAR system with M subapertures increases the storage capacity by a factor of M, which is counteracted by the low PRF. For the proposed system, the low storage capacity brought by the low PRF is increased by a factor of N_{ant}, the number of antenna elements. Generally, N_{ant} is greater than M, so the proposed system can be realized until the storage capabilities have been greatly developed.

Another disadvantage is the low energy efficiency resulting from the divergence of vortex beams. To obtain a linear phase history, only one part of the main lobe of the vortex beam is utilized, and the other parts are wasted. The introduction of the linear phase history by vortex beams also creates two unavoidable problems. One problem is the phase history that varies with the distance gate, and the other problem is the higher order phase that is difficult to eliminate. One can solve the problems by generating beams with a very pure linear phase in the main lobe instead of vortex beams.

B. Alternative Proposals

Based on the limitations of the current storage technology and the characteristics of the 2-D space-varying vortex phase, we propose two alternative proposals to implement the method proposed in this article. The two proposals are alternate pulse reception and beams with a linear phase in the main lobe. Both proposals are immature at present and plans for future work.

1) Alternate Pulse Reception: One way to alleviate the storage pressure of the system is to alternately control the receiving pattern using vortex beams with different modes, as shown in Fig. 11, which depicts the principle of alternate three pulse reception. The transmitting pattern is an ordinary beam with OAM mode $L = 0$. In the first receiving window, the phase of Rx is controlled to generate a vortex beam with the L_1 mode, and the main lobe with a linear phase in the azimuth is located in the swath. Then, the L_2 mode is used to receive the echo in the following receiving window, followed by the L_3 mode and then by another three modes in the three receiving windows, and so on.

This approach needs to change the phase distribution of the antenna elements in each receiving window but avoids storing a large amount of data. There is no need to increase

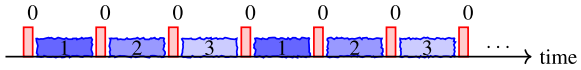

Fig. 11. Principle of alternate pulse reception. The red filled rectangles represent transmitting pulses. The blue filled rectangles represent receiving pulses. The number 0 denotes the transmitting pattern with OAM mode $L = 0$. The numbers 1, 2, and 3 denote receiving patterns with OAM modes $L = L_1, L_2$, and L_3, respectively, where $L_1 \neq L_2 \neq L_3 \neq 0$.

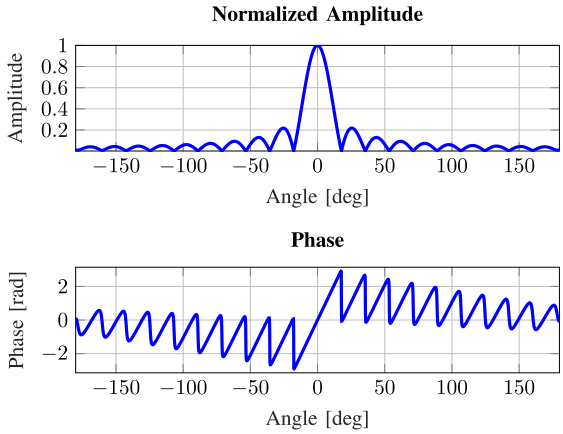

Fig. 12. Desired pencil beam with a linear phase in the main lobe. (Top and Bottom) Normalized amplitude and phase, respectively.

the antenna aperture due to the utilization of the linear phase in the azimuth of the vortex beams. However, the PRF of the whole system with this approach cannot be reduced because the PRF of the same receiving mode is 1/3 of that of the transmitting pulses due to alternating pulses.

2) Beams With Linear Phase in the Main Lobe: The introduction of a linear phase in the vortex beam also produces some problems, such as the divergence of the main lobe, the phase history varying with the range gate, and the existence of higher order phases. One possible solution is to design a pencil beam whose phase changes linearly in the main lobe, as shown in Fig. 12. From another perspective, a pencil beam has an oblique wavefront, which enables a virtual receiving aperture, as described in Section III-B.

It is necessary to design different slopes of linear phase beams instead of vortex OAM modes. The phase history varying with the range gate and higher order phase will be resolved, so the signal reconstruction will not be adversely affected.

VI. Conclusion

In this article, a novel SAR system was proposed to reduce the PRF of the system without increasing the antenna aperture compared with an azimuth multichannel SAR system. Vortex beams with different OAM modes played an important role, i.e., providing multiple linear phases in the azimuth echoes, similar to multiple virtual receiving positions. The positions of the virtual Rxs, related to the OAM modes and the azimuth aperture of the Tx, were deduced from both the perspective of signal analysis and the perspective of the wavefront. The virtual multi-Rx SAR system resembles an azimuth multichannel SAR system, which is intended to decrease the system PRF.

$$\tilde{\boldsymbol{H}}(f_\eta) = \begin{bmatrix} e^{j\omega_\eta \eta_{L_1}} e^{-j\varphi_{L_1}} & e^{j\omega_\eta \eta_{L_2}} e^{-j\varphi_{L_2}} & \cdots & e^{j\omega_\eta \eta_{L_N}} e^{-j\varphi_{L_N}} \\ e^{j(\omega_\eta+\omega_\sigma)\eta_{L_1}} e^{-j\varphi_{L_1}} & e^{j(\omega_\eta+\omega_\sigma)\eta_{L_2}} e^{-j\varphi_{L_2}} & \cdots & e^{j(\omega_\eta+\omega_\sigma)\eta_{L_N}} e^{-j\varphi_{L_N}} \\ \vdots & \vdots & \ddots & \vdots \\ e^{j(\omega_\eta+(N-1)\omega_\sigma)\eta_{L_1}} e^{-j\varphi_{L_1}} & e^{j(\omega_\eta+(N-1)\omega_\sigma)\eta_{L_2}} e^{-j\varphi_{L_2}} & \cdots & e^{j(\omega_\eta+(N-1)\omega_\sigma)\eta_{L_N}} e^{-j\varphi_{L_N}} \end{bmatrix} \tag{40}$$

$$= \begin{bmatrix} 1 & 1 & \cdots & 1 \\ e^{j\omega_\sigma \eta_{L_1}} & e^{j\omega_\sigma \eta_{L_2}} & \cdots & e^{j\omega_\sigma \eta_{L_N}} \\ \vdots & \vdots & \ddots & \vdots \\ e^{j(N-1)\omega_\sigma \eta_{L_1}} & e^{j(N-1)\omega_\sigma \eta_{L_2}} & \cdots & e^{j(N-1)\omega_\sigma \eta_{L_N}} \end{bmatrix} \cdot \begin{bmatrix} e^{j\omega_\eta \eta_{L_1}} e^{-j\varphi_{L_1}} & 0 & \cdots & 0 \\ 0 & e^{j\omega_\eta \eta_{L_2}} e^{-j\varphi_{L_2}} & \cdots & 0 \\ \vdots & \vdots & \ddots & \vdots \\ 0 & 0 & \cdots & e^{j\omega_\eta \eta_{L_N}} e^{-j\varphi_{L_N}} \end{bmatrix} \tag{41}$$

The main steps of the proposed system are repeated here. First, multiple proper OAM modes are preselected for the receiving pattern according to various conditions. Next, the antenna transmits an $L = 0$ mode vortex beam and then receives and stores each echo with an $L = 0$ receiving pattern under a low PRF. Each echo is multiplied by multiple-phase distributions based on preselected OAM modes L to obtain echoes equivalently received by virtual Rxs. Finally, a signal reconstruction algorithm is applied to recover the spectrum of the aliased signals, followed by a general SAR imaging algorithm.

The simulation results are perfect for two and three modes. However, for higher modes, the results become worse due to the inherent characteristics of the vortex beam. To solve this problem, it is helpful to design and generate a pencil beam with a linear phase in the main lobe. On the other hand, to alleviate the huge data storage requirement, an alternate pulse receiving scheme can be considered. Future work will focus on these two aspects and conducting real outdoor experiments.

APPENDIX

In this appendix, the condition for $\tilde{\boldsymbol{H}}(f_\eta)$ to be invertible is derived. Recalling the transfer function (20)

$$H_L(f_\eta) = \exp(-j2\pi \eta_L f_\eta) \cdot \exp(-j\varphi_L). \tag{34}$$

For simplicity and shortening the formulas, let

$$\omega_\eta = -2\pi f_\eta, \quad \omega_\sigma = -2\pi\sigma \tag{35}$$

where $\sigma = \text{PRF}$ and $f_\eta \subset [-B_a/2, -B_a/2 + \sigma]$. Then, the system transfer matrix for vortex multimode system (21) can be written as (40), as shown at the top of the page and expanded as (41), as shown at the top of the page.

In (41), the first matrix is a Vandermonde matrix and the second matrix is a diagonal matrix, so the determinant of $\tilde{\boldsymbol{H}}(f_\eta)$ can be expressed as

$$\det\left(\tilde{\boldsymbol{H}}\right) = e^{j\omega_\eta\left(\eta_{L_1}+\eta_{L_2}+\cdots+\eta_{L_N}\right)} e^{-j\left(\varphi_{L_1}+\varphi_{L_2}+\cdots+\varphi_{L_N}\right)} \cdot \prod_{1\leqslant i<j\leqslant N} \left(e^{j\omega_\sigma \eta_{L_i}} - e^{j\omega_\sigma \eta_{L_j}}\right). \tag{36}$$

$\tilde{\boldsymbol{H}}(f_\eta)$ is an invertible matrix if and only if $\det\left(\tilde{\boldsymbol{H}}\right) \neq 0$, that is, for all $i \neq j$ and any integer $k \in \mathbb{Z}$

$$\omega_\sigma \eta_{L_i} \neq \omega_\sigma \eta_{L_j} - 2k\pi \tag{37}$$

$$\Leftrightarrow -2\pi\sigma \frac{F_{L_i}}{K_a} \neq -2\pi\sigma \frac{F_{L_j}}{K_a} - 2k\pi. \tag{38}$$

Substituting $\sigma = \text{PRF} = B_a/N$ and $K_a = B_a/T_s$ into (38), we obtain the invertible condition

$$F_{L_i} \neq F_{L_j} + \frac{kN}{T_s} \tag{39}$$

REFERENCES

[1] Y.-K. Deng, F.-J. Zhao, and Y. Wang, "Brief analysis on the development and application of spaceborne SAR," *J. Radars*, vol. 1, no. 1, pp. 1–10, Jul. 2012.

[2] C. A. Wiley, "Pulsed Doppler radar methods and apparatus," Goodyear Aerosp. Corp., Akron, OH, USA, Tech. Rep. 3196436, Jul. 1965.

[3] C. A. Wiley, "Synthetic aperture radars," *IEEE Trans. Aerosp. Electron. Syst.*, vol. AES-21, no. 3, pp. 440–443, May 1985.

[4] G. Krieger, M. Younis, N. Gebert, F. Bordoni, A. Patyuchenko, and A. Moreira, "Advanced concepts for high-resolution wide-swath SAR imaging," in *Proc. Eur. Conf. Synth. Aperture Radar*, Aachen, Germany, Jun. 2010, pp. 1–4.

[5] R. Sullivan, *Microwave Radar: Imaging and Advanced Concepts*. Norwood, MA, USA: Artech House, 2000.

[6] I. G. Cumming and F. H. Wong, *Digital Processing of Synthetic Aperture Radar Data*. Norwood, MA, USA: Artech House, 2005.

[7] N. Gebert, G. Krieger, and A. Moreira, "Digital beamforming on receive: Techniques and optimization strategies for high-resolution wide-swath SAR imaging," *IEEE Trans. Aerosp. Electron. Syst.*, vol. 45, no. 2, pp. 564–592, Apr. 2009.

[8] N. Gebert, "Multi-channel azimuth processing for high-resolution wide-swath SAR imaging," Ph.D. dissertation, Fakultät Elektrotechnik und Informationstechnik (ETIT), Institut Für Hochfrequenztechnik und Elektronik (IHE), Karlsruhe, Germany, 2009.

[9] A. Papoulis, "Generalized sampling expansion," *IEEE Trans. Circuits Syst.*, vol. CAS-24, no. 11, pp. 652–654, Nov. 1977.

[10] M. Younis, "Digital beam-forming for high-resolution wide swath real and synthetic aperture radar," Ph.D. dissertation, Fak. für Elektrotech., Univ. Karlsruhe, Karlsruhe, Germany, 2004.

[11] M. Younis, S. Huber, A. Patyuchenko, F. Bordoni, and G. Krieger, "Performance comparison of reflector-and planar-antenna based digital beam-forming SAR," *Int. J. Antennas Propag.*, vol. 2009, Jun. 2009, Art. no. 614931.

[12] M. Younis, C. Fischer, and W. Wiesbeck, "Digital beamforming in SAR systems," *IEEE Trans. Geosci. Remote Sens.*, vol. 41, no. 7, pp. 1735–1739, Jul. 2003.

[13] W. Xu, P. Huang, and Y.-K. Deng, "Multi-channel SPCMB-tops SAR for high-resolution wide-swath imaging," *Prog. Electromagn. Res.*, vol. 116, pp. 533–551, 2011.

[14] D. Cerutti-Maori, I. Sikaneta, J. Klare, and C. H. Gierull, "MIMO SAR processing for multichannel high-resolution wide-swath radars," *IEEE Trans. Geosci. Remote Sens.*, vol. 52, no. 8, pp. 5034–5055, Aug. 2014.

[15] I. Sikaneta, C. H. Gierull, and D. Cerutti-Maori, "Optimum signal processing for multichannel SAR: With application to high-resolution wide-swath imaging," *IEEE Trans. Geosci. Remote Sens.*, vol. 52, no. 10, pp. 6095–6109, Oct. 2014.

[16] L. Guangyan, W. Youlin, and L. Youquan, "Unambiguous reconstruction and imaging of nonuniform sampling SAR signals," in *Proc. 1st Asian Pacific Conf. Synth. Aperture Radar*, Nov. 2007, pp. 253–256.

[17] B. Liu and Y. He, "Improved DBF algorithm for multichannel high-resolution wide-swath SAR," *IEEE Trans. Geosci. Remote Sens.*, vol. 54, no. 2, pp. 1209–1225, Feb. 2016.
[18] N. Liu, R. Wang, Y. Deng, S. Zhao, and X. Wang, "Modified multi-channel reconstruction method of SAR with highly nonuniform spatial sampling," *IEEE J. Sel. Topics Appl. Earth Observ. Remote Sens.*, vol. 10, no. 2, pp. 617–627, Feb. 2017.
[19] C. Fang, Y. Liu, Z. Suo, Z. Li, and J. Chen, "Improved channel mismatch estimation for multi-channel HRWS SAR based on azimuth cross-correlation," *Electron. Lett.*, vol. 54, no. 4, pp. 235–237, Feb. 2018.
[20] H. Gao, J. Chen, S. Quegan, W. Yang, and C. Li, "Parameter estimation and error calibration for multi-channel beam-steering SAR systems," *Remote Sens.*, vol. 11, no. 12, p. 1415, Jun. 2019.
[21] Y. Zhou *et al.*, "A novel approach to Doppler centroid and channel errors estimation in azimuth multi-channel SAR," *IEEE Trans. Geosci. Remote Sens.*, vol. 57, no. 11, pp. 8430–8444, Nov. 2019.
[22] X. Ma, Z. Sun, Z. Dong, and H. Huang, "Azimuth ambiguity of multi-channel SAR," in *Proc. IEEE Int. Geosci. Remote Sens. Symp.*, Jul. 2012, pp. 3807–3810.
[23] S.-X. Zhang, M.-D. Xing, X.-G. Xia, Y.-Y. Liu, R. Guo, and Z. Bao, "A robust channel-calibration algorithm for multi-channel in azimuth HRWS SAR imaging based on local maximum-likelihood weighted minimum entropy," *IEEE Trans. Image Process.*, vol. 22, no. 12, pp. 5294–5305, Dec. 2013.
[24] L. Guo, X. Tan, and H. Dang, "Range ambiguity suppression for multi-channel SAR system near singular points," in *Proc. IEEE Int. Geosci. Remote Sens. Symp. (IGARSS)*, Jul. 2016, pp. 2086–2089.
[25] R. C. Devlin, A. Ambrosio, N. A. Rubin, J. P. B. Mueller, and F. Capasso, "Arbitrary spin-to-orbital angular momentum conversion of light," *Science*, vol. 358, no. 6365, pp. 869–901, 2017.
[26] B. Thidé *et al.*, "Utilization of photon orbital angular momentum in the low-frequency radio domain," *Phys. Rev. Lett.*, vol. 99, no. 8, Aug. 2007, Art. no. 087701.
[27] G. Shu *et al.*, "Chirp signal transmission and reception with orbital angular momentum multiplexing," *IEEE Antennas Wireless Propag. Lett.*, vol. 18, no. 5, pp. 986–990, May 2019.
[28] K. Liu, Y. Cheng, X. Li, H. Wang, Y. Qin, and Y. Jiang, "Study on the theory and method of vortex-electromagnetic-wave-based radar imaging," *IET Microw., Antennas Propag.*, vol. 10, no. 9, pp. 961–968, Jun. 2016.
[29] B. Tang, K.-Y. Guo, J.-P. Wang, and X.-Q. Sheng, "Resolution performance of the orbital-angular-momentum-based imaging radar," *IEEE Antennas Wireless Propag. Lett.*, vol. 16, pp. 2975–2978, 2017.
[30] K. Liu, Y. Gao, X. Li, and Y. Cheng, "Target scattering characteristics for OAM-based radar," *AIP Adv.*, vol. 8, no. 2, 2018, Art. no. 025002.
[31] S. Guo, Z. He, Z. Fan, and R. Chen, "CUCA based equivalent fractional order OAM mode for electromagnetic vortex imaging," *IEEE Access*, vol. 8, pp. 91070–91075, 2020.
[32] T. Yang, S. Li, O. Xu, W. Li, and Y. Wang, "Three dimensional SAR imaging based on vortex electromagnetic waves," *Remote Sens. Lett.*, vol. 9, no. 4, pp. 343–352, Apr. 2018.
[33] Y. Fang *et al.*, "A novel SAR imaging method based on electromagnetic vortex with orbital-angular-momentum," in *Proc. IEEE Int. Geosci. Remote Sens. Symp. (IGARSS)*, Jul. 2017, pp. 1638–1641.
[34] Y. Fang, J. Chen, P. Wang, Z. Men, X. Zhou, and K. Hu, "A novel imaging formation of electromagnetic vortex SAR with time-variant orbital-angular-momentum," in *Proc. IEEE Int. Geosci. Remote Sens. Symp. IGARSS*, Jul. 2018, pp. 577–580.
[35] J. Wang, K. Liu, Y. Cheng, and H. Wang, "Vortex SAR imaging method based on OAM beams design," *IEEE Sensors J.*, vol. 19, no. 24, pp. 11873–11879, Dec. 2019.
[36] X. Bu, Z. Zhang, L. Chen, X. Liang, H. Tang, and X. Wang, "Implementation of vortex electromagnetic waves high-resolution synthetic aperture radar imaging," *IEEE Antennas Wireless Propag. Lett.*, vol. 17, no. 5, pp. 764–767, May 2018.
[37] M. Barbuto, F. Trotta, F. Bilotti, and A. Toscano, "Circular polarized patch antenna generating orbital angular momentum," *Prog. Electromagn. Res.*, vol. 148, pp. 23–30, 2014.
[38] S. M. Mohammadi *et al.*, "Orbital angular momentum in radio: A system study," *IEEE Trans. Antennas Propag.*, vol. 58, no. 2, pp. 565–572, Feb. 2010.
[39] C. A. Balanis, *Antenna Theory: Analysis and Design*. Hoboken, NJ, USA: Wiley, 2016.

Gaofeng Shu received the B.S. degree from Wuhan University, Wuhan, Hubei, China, in 2015. He is pursuing the Ph.D. degree with the Department of Space Microwave Remote Sensing Systems, Aerospace Information Research Institute, Chinese Academy of Sciences, Beijing, China.

He is with the University of Chinese Academy of Sciences, Beijing. His research interests include synthetic aperture radar (SAR) imaging, orbital angular momentum (OAM), and electromagnetic vortex technology in synthetic aperture radar (SAR) systems.

Nan Wang was born in Tianjin, China, in 1973. He received the B.S. degree in electromagnetic fields and microwave technology from Xidian University, Xi'an, China, in 1996, and the Ph.D. degree in electromagnetic fields and microwave technology from the Beijing Institute of Technology, Beijing, China, in 2008.

He is an Associate Research Fellow with the Institute of Electronics, Chinese Academy of Sciences, Beijing. His research interests include broadband antenna, array antenna, synthetic aperture radar system, and antenna near-field measurement.

Wentao Wang received the B.S. and M.S. degrees in electromagnetic and microwave technology from the University of Electronic Science and Technology of China, Chengdu, China, in 2012 and 2015, respectively. He is pursuing the D.Eng. degree in electronics and information with Northwestern Polytechnical University, Xi'an, China.

He is an Assistant Research Fellow with the Aerospace Information Research Institute, Chinese Academy of Sciences, Beijing, China. His research interests include broadband antenna, phased array antenna, and electromagnetic vortex technology in synthetic aperture radar systems.

Yunkai Deng (Member, IEEE) received the M.S. degree in electrical engineering from the Beijing Institute of Technology, Beijing, China, in 1993.

In 1993, he joined the Institute of Electronics, Chinese Academy of Sciences (IECAS), Beijing, where he was involved in antenna design, microwave circuit design, and spaceborne/airborne synthetic aperture radar (SAR) technology. He has been the Leader of several spaceborne/airborne SAR programs and developed some key technologies of spaceborne/airborne SAR. He is a Research Scientist and a member of the Scientific Board. Since 2012, he has been a Principal Investigator with the Helmholtz-CAS Joint Research Group concerning Space-borne Microwave Remote Sensing for Prevention and Forensic Analysis of Natural Hazards and Extreme Events. He has authored or coauthored more than 100 articles since 2002, of which more than 100 peer-reviewed and well-known journal articles. His research interests include spaceborne/airborne SAR technology for advanced modes, multifunctional radar imaging, and microwave circuit design.

Dr. Deng was rewarded several prizes, including the first and second class rewards of National Defense Science and Technology Progress in 2007, the first class reward of National Scientific and Technological Progress in 2008, the achievements of outstanding award of CAS in 2009, and the first-class reward of army science and technology innovation in 2016, for his outstanding contribution in SAR field.

Yongwei Zhang received the B.S. degree in mathematics and physics basic science from the University of Electronic Science and Technology of China, Chengdu, China, in 2015, and the Ph.D. degree in communication and information system from the Graduate University of Chinese Academy of Sciences, Beijing, China, in 2020.

In 2020, he joined the Institute of Electronics, Chinese Academy of Sciences (IECAS), Beijing, where he was involved in synthetic aperture radar (SAR) encoding technology and application. His research interests include multichannel SAR and multi-input–multioutput (MIMO) SAR system design and signal processing, and waveform diversity.

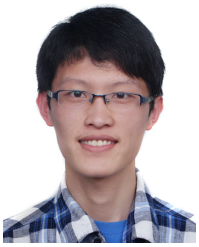

Heng Zhang (Member, IEEE) received the B.S. degree from Nanjing University, Nanjing, China, in 2013, and the Ph.D. degree in communication and information systems from the University of Chinese Academy of Sciences, Beijing, China, in 2018.

In 2018, he joined the Aerospace Information Research Institute, Chinese Academy of Sciences. His research interests include bistatic synthetic aperture radar imaging and interferometry.

Ning Li (Member, IEEE) received the B.S. degree in electronics information engineering from Northeast Forestry University, Harbin, China, in 2009, the M.S. degree in communication and information system from the Nanjing University of Aeronautics and Astronautics, Nanjing, China, in 2012, and the Ph.D. degree from the Institute of Electronics, Chinese Academy of Sciences (IECAS), Beijing, China, in 2015.

In 2015, he joined the Department of Space Microwave Remote Sensing System, IECAS, where he was an Assistant Professor. Since 2017, he has been a Full Professor with the School of Computer and Information Engineering, Henan University, Kaifeng, China. His research interests include synthetic aperture radar (SAR) and inverse SAR imaging algorithms and autofocusing techniques, SAR polarimetric theory, and SAR image processing.

Dr. Li was a recipient of the Special Prize of President Scholarship for Postgraduate Students from the University of Chinese Academy of Sciences in 2015.

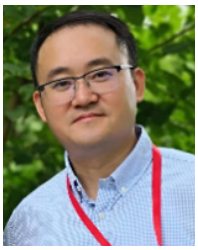

Robert Wang (Senior Member, IEEE) received the B.S. degree in control engineering from Henan University, Kaifeng, China, in 2002, and the Dr.Eng. degree from the Graduate University of Chinese Academy of Sciences, Beijing, China, in 2007.

In 2007, he joined the Center for Sensor Systems (ZESS), University of Siegen, Siegen, Germany. He was involved in various joint projects supported by ZESS and Fraunhofer-FHR, Wachtberg, Germany, e.g., the TerraSAR-X/phased array multifunctional imaging radar (PAMIR) hybrid bistatic synthetic aperture radar (SAR) experiment, the PAMIR/stationary bistatic SAR experiment, the PAMIR/stationary bistatic SAR experiment with nonsynchronized oscillator, and the millimeter-wave frequency modulated continuous wave (FMCW) SAR data processing. Since 2011, he has been a Research Fellow with the Spaceborne Microwave Remote Sensing System Department, Institute of Electronics, Chinese Academy of Sciences (IECAS), where he has been funded by the Hundred Talents Program of the Chinese Academy of Sciences. Since 2012, he has been a Co-Principal Investigator (PI) with the Helmholtz-CAS Joint Research Group, Beijing, concerning spaceborne microwave remote sensing for prevention and forensic analysis of natural hazards and extreme events. He is also responsible for several national high-resolution spaceborne imaging radar missions supported by the National High-Resolution Earth Observation Major Special Program. He is also the PI of two advanced L-band spaceborne SAR systems that are aimed at global dynamic earth monitoring. He has authored or coauthored more than 100 peer-reviewed journal articles in the field of SAR imaging technology and published the book, *Bistatic SAR System and Signal Processing Technology* (Springer). His research interests include monostatic and multistatic SAR imaging and high-resolution wide-swath spaceborne SAR system and imaging models.

Dr. Wang was a recipient of the National Ten Thousand Talent Program-Young Top-Notch Talent Program Award in 2014 and the National Natural Science Funds of China for Excellent Young Scholar in 2014. He received the Zhao Jiuzhang Award for Outstanding Young Science in 2015, the First Prize for Military Scientific and Technological Progress in 2016, the Scientific and Technological Innovation Leading Talent by National High-Level Talents Special Support Plan in 2017, and the Distinguished Young Scholars from the National Natural Science Foundation of China in 2018. He was the Session Chair for the European Conference on Synthetic Aperture Radar (EUSAR) and the International Geoscience and Remote Sensing Symposium (IGARSS) from 2012 to 2016. He has contributed to invited sessions at the EUSAR from 2008 to 2016, the European Radar Conference in 2009, and IGARSS from 2012 to 2016. He has been an Associate Editor of the IEEE TRANSACTIONS ON GEOSCIENCE AND REMOTE SENSING since 2020.